Advanced Powder Technology 31 (2020) 70–77

Contents lists available at ScienceDirect

Advanced Powder Technology

journal homepage: www.elsevier.com/locate/apt

Original Research Paper

High performance zeolitic imidazolate framework-8 (ZIF-8) based suspension: Improving the shear thickening effect by controlling the morphological particle-particle interaction

Yuxuan Wu [a], Saisai Cao [a], Shouhu Xuan [a,*], Min Sang [b], Linfeng Bai [b], Sheng Wang [a], Junshuo Zhang [a], Yu Wang [a], Wanquan Jiang [b], Xinglong Gong [a,*]

[a] CAS Key Laboratory of Mechanical Behavior and Design of Materials, Department of Modern Mechanics, CAS Center for Excellence in Complex System Mechanics, University of Science and Technology of China, Hefei, Anhui 230027, China
[b] Department of Chemistry, University of Science and Technology of China, Hefei, Anhui 230026, China

ARTICLE INFO

Article history:
Received 19 August 2019
Received in revised form 24 September 2019
Accepted 1 October 2019
Available online 17 October 2019

Keywords:
Shear thickening fluid
ZIF-8
Adsorption
Rheology
Friction

ABSTRACT

A novel shear thickening fluid (Z-STF) was developed *via* dispersing zeolitic imidazolate framework-8 (ZIF-8) nanoparticles into ethylene glycol (EG). By varying the morphologies of the ZIF-8 nanoparticles, the rheological properties of the Z-STF were controlled. In comparison to the traditional SiO_2 based STF (S-STF), the Z-STF showed a superior shear thickening behavior because of the porous nature and polyhedron morphology of the ZIF-8 nanoparticles. Firstly, the EG molecule could be incorporated into the micropores of ZIF-8, which increased the volume fraction of the dispersing phases and enhanced the hydrodynamic forces between the particles. Secondly, the poor relative sliding of truncated cubic particles led to easily form a more robust structure of frictional contact network in truncated cube ZIF-8 based STF (TCZ-STF) than in truncated rhombic dodecahedron ZIF-8 based STF (TRDZ-STF) and S-STF, thus the TCZ-STF showed smaller critical shear rates and higher maximum viscosities. This work provides a morphology turning method to design high performance STF and supplies a good understanding of the relationship between ST behavior and particles' structure. In view of the easy preparation and wonderful mechanical properties, the Z-STF possessed broad application in damping, body armor, and safe energy.

1. Introduction

Shear thickening fluid (STF) is a kind of non-Newtonian fluid whose viscosity increases with an applied shear rate once the shear rate comes up to its critical value [1–3]. Because of the interesting shear thickening property, STF is suitable for many applications, such as liquid body armor, shock absorbers, sports shoe cushioning, and etc. [4–6]. Particularly, STF treated fabrics used for body protective applications are widely studied in recent years [7–10]. Cwalina et al. [9] demonstrated that aramid textiles intercalated with STF can endow a great enhancement to the garment's cut and puncture resistance. STF consists of a dispersing phase and a dispersing media. The most common STF is prepared by dispersing silica into ethylene glycol (EG) or polyethylene glycol. The properties of STF are highly dependent on the dispersing phase, the dispersing media, and the additives, in which the dispersing phase is the most important factor. Changing the dispersing phase, such as volume fraction, particle size, size distribution, shape, and surface chemistry properties, can dramatically influence the rheological properties of STF [11,12]. Generally, shear thickening is easier to occur at high volume fractions. In the case of equal volume fractions, the larger the particle size, the smaller the critical shear rate [13,14]. Egres et al. [15] studied the influence of particles' shape on the ST properties of STF. They found that shear thickening was more likely to occur when the dispersing phase was composed of anisotropic particles. The suspension of rod-shaped particles was most prone to show shear thickening behavior, followed by plate particles, while the viscosity of spherical particles STF was the smallest.

Various mechanisms, such as order-disorder transition, hydrocluster, and contact rheology model, have been developed to explain the ST behavior. Studies have shown that the interparticle stress was too small to exceed interparticle repulsion at low shear

* Corresponding authors.
E-mail addresses: xuansh@ustc.edu.cn (S. Xuan), gongxl@ustc.edu.cn (X. Gong).

https://doi.org/10.1016/j.apt.2019.10.001

rates and the shear thickening could be explained by the formation of hydrocluster [16,17]. The interaction between dispersed particles and solvent molecules was a vital factor for the formation of hydrocluster [18]. In fact, hydrodynamic mechanism only explained the mild viscosity increase at the onset of thickening, but was not suitable for the discontinuous shear thickening (DST) [19–21]. Many simulation calculations proved that the formation of friction contact networks was the main reason for the emergence of DST in STF [22,23]. Pednekar et al. [24] believed that the particles had good dispersibility in the pure Brown state. Once the attraction force was introduced in simulation, the friction contact network formed by particles would have the ability to withstand the applied shear forces, resulted in an increase in suspension viscosity and yield stress. In addition, it was found that the friction played an important role in shear thickening. Hsiao et al. [25] studied the rheological properties of concentrated colloidal suspensions with particles having different surface roughness. They found that the volume fraction and critical stress required for shear thickening were reduced with the increase of particle surface roughness, and the results obtained by adjusting the friction coefficient of the particles during the simulation were consistent with the experimental results. Hsu et al. [26] measured the sliding of the particles by lateral force microscopy and determined that the interaction of the rough surface was a "stick-slip" frictional contact. It was confirmed that the friction between the solid particles was very important in adjusting the shear thickening performance of the suspension.

Zeolitic imidazolate framework-8 is formed by bridging Zn^{2+} with 2-methylimidazole, which exhibits sodalite (SOD) zeolite-type structure and has large cavities (11.6 Å) and small pore apertures (3.4 Å). It possesses a large microporous volume of about 0.6 cm^3/g and has a low density of nearly 1 g/cm^3 [27–29]. The ZIF-8 is widely used in fields of adsorption and gas separation for its high porosities and large surface areas [30–32]. Due to its low density, suspensions prepared from ZIF-8 would reduce the total mass dramatically at the same volume fraction, which would facilitate their practical applications in flexible body protective applications and improve the economic efficiency of industrial processes. The high surface area and rough surface of ZIF-8 may affect the interaction between the particles as well as the interaction between the particles and the dispersing media. As a result, the ST effect is changed. In addition, ZIF-8 is thermally stable (up to 550 °C in N_2) and has exceptional chemical resistance to boiling alkaline solution, water and organic solvents, such as methanol, benzene et al. [33] Moreover, it is important to recognize that ZIF-8 displays good mechanical behaviors, which is hopeful to work under considerable stresses and pressures [29]. By controlling the reaction conditions, various crystal morphologies of ZIF-8, such as sphere, nanosheet, rhombic dodecahedron, cube, and other polyhedrons, can be synthesized [34–37]. Because of the porosity of ZIF-8, dispersing ZIF-8 in water or aqueous electrolyte solutions could form a "zeosil-water" system, which could be used for storage/restoration of mechanical energy. During the compression step, solutions intruded into the micropores of ZIF-8 by absorbing mechanical energy. When the pressure was released, solutions extruded from the micropores and hence behaved like a spring, shock-absorber or bumper [38]. Considering ZIF-8's excellent chemical and thermal stability, porous structure, tunable microscopic morphology, and controllable surface properties, it is expected that ZIF-8 can be used as a dispersing phase of STF to optimize the ST behavior and deepen the understanding between ST behavior and particles' structure.

In this work, ZIF-8 was used as the dispersing phase for the first time to prepare high performance STF. Truncated cube ZIF-8 (TC ZIF-8) and truncated rhombic dodecahedron ZIF-8 (TRD ZIF-8) nanoparticles were synthesized by controlling the reaction conditions, such as time, the concentration of reactants and CTAB. The ZIF-8's structure dependent ST behaviors of Z-STF were systematically investigated. Compared to TRDZ-STF and S-STF, TCZ-STF exhibited better ST properties. On the one hand, the EG molecules could be incorporated into the micropores to enhance the hydrodynamic forces among the ZIF-8 nanoparticles. On the other hand, the polyhedron morphology increased the interface frictions. This work provides a new approach to designing high performance STFs and supplies a good understanding of the relationship between ST behavior and particle structure. In addition, as a novel shear thickening system, ZIF-8 based STFs broaden the application of STF in damping, ballistic and safe energy.

2. Material and methods

2.1. Materials

All chemicals were from commercial sources and used without further purification: zinc acetate dihydrate (AR), hexadecyltrimethyl-ammonium bromide (CTAB, AR), Tetraethylorthosilicate (TEOS, liquid, CP), ammonium hydroxide ($NH_3{\cdot}H_2O$, liquid, 25–28%, AR), ethylene glycol (EG, AR), and ethanol (AR) were purchased from Sinopharm Chemical Reagent Co., Ltd; 2-methylimidazole (2-MiM, 99%) were purchased from Beijing Bailingwei Technology Co., Ltd.

2.2. Preparation of ZIF-8 and SiO_2 particles

ZIF-8 was prepared through an approach reported before with some modifications [34] and SiO_2 nanospheres were synthesized *via* the modified Stöber sol–gel method.

2.2.1. Synthesis of TC ZIF-8 particles

Briefly, 14.4 g $Zn(CH_3COO)_2{\cdot}2H_2O$ was dissolved in 240 mL of water (solution 1). In another beaker, 53.6 g 2-MiM and varying amounts of CTAB were dissolved in 240 mL of water (solution 2). Pouring solution 1 into solution 2 quickly and stirring for a few seconds. The resulting mixture was left undisturbed at 25 °C for 2 h, following washed three times with ethanol to get the resulting ZIF-8 particles. The obtained ZIF-8 nanoparticles were finally activated at 100 °C overnight under vacuum. To synthesize different size of ZIF-8 nanoparticles, varying concentrations of CTAB were used: for 240 nm, [CTAB] = 0.54 mM; for 300 nm, [CTAB] = 0.44 mM.

2.2.2. Synthesis of TRD ZIF-8 particles

Firstly, 9.4 g $Zn(CH_3COO)_2{\cdot}2H_2O$ dissolved in 156 mL of water (solution 1). In another beaker, 44.7 g 2-MiM was dissolved in water to obtain a 200 mL transparent solution (solution 2). Pouring solution 1 into solution 2 quickly and stirring for a few seconds. The resulting mixture was left undisturbed at 25 °C for 1 h, following washed three times with ethanol to get the resulting ZIF-8 particles. The obtained ZIF-8 nanoparticles were finally heated at 100 °C overnight under vacuum to activate.

2.2.3. Preparation of the STF

A certain amount of EG was added to a beaker. Then the calculated mass of ZIF-8 (or SiO_2) was slowly added to EG and dispersed by stirring for 30 min. The suspension systems were then ultrasonicated for another 4 h to obtain the Z-STF (or S-STF).

2.3. Characterization

The rheological properties of the STF were tested using Anton Paar's Physical MCR302 at 25 °C. The microstructures of ZIF-8

and SiO_2 were characterized using an environmental scanning electron microscope (SEM, Philips of Holland, model XL30 ESEM-TMP) under 3 kV, and a transmission electron microscopy (TEM, HT7700, Japan) under 100 kV. X-ray diffraction (XRD) patterns were collected on an X-ray diffractometer (XRD, Smartlab, Rigaku, Japan) with Cu Kα radiation (λ = 1.54178 Å). The infrared (IR) spectra of the samples were obtained by the Nicolet Model 759 Fourier transform infrared (FT-IR) spectrometer in the wavenumber range from 4000 to 400 cm^{-1} with a KBr wafer. The thermal stabilities of the samples were tested from room temperature to 700 °C under N_2 flow for balance and purge gases, which was investigated by a DTG-60H. A Micromeritics Tristar II 3020 M was employed to record the Brunauer-Emmett-Teller (BET) surface area and pore volume of the samples. Before the tests, all of the samples were activated at 100 °C for 5 h under vacuum. The surface composition of the samples was obtained from X-ray photoelectron spectroscopy (XPS), which was carried by ESCALAB250. Before these tests, TRDZ-STF was dried at 168 °C to obtain samples, which was denoted as ZIF-8/EG.

3. Results and discussion

300 nm TC ZIF-8 nanoparticles are synthesized firstly (diameter defined as the distance between opposing square facets), and they exhibit uniform size as shown in Figs. 1a–c and S1. It should be pointed out that the nanoparticles can be prepared in large-scale and around 13 g TC ZIF-8 is obtained by one reaction. Generally, the ZIF-8 seeds formed in the initial stage are cubic, and the subsequent evolution is dominated by (1 0 0) growth, resulting in rhombohedral dodecahedral crystals, which are thermodynamically stable [39,40]. In this paper, the widely used cationic surfactant CTAB acted as a capping agent, which selectively adsorbed on the {1 0 0} facets during the crystallization [36]. As a result, the truncated cube ZIF-8 was obtained. X-ray diffraction pattern (XRD, Fig. 1d) shows that the samples have sharp peaks which match the ideal simulated XRD of ZIF-8, indicating that the obtained product is crystallized ZIF-8. After dispersing the ZIF-8 into the EG, the 300 nm CTZ-STF is obtained. Fig. 1e presents the static rheological properties of the 300 nm CTZ-STF. It is clear that with the increase of volume fraction, the critical shear rates reduce and the maximum viscosities increase. These results indicate that the ST behavior becomes better with the increase of the ZIF-8 volume fraction.

By increasing the CTAB concentration to 0.54 mM, 240 nm TC ZIF-8 nanoparticles were synthesized. As shown in Figs. 2(a, d), and S1, TC ZIF-8 retained the truncated cube microstructure, and the size was smaller than the above one. It is reported that when more CTAB is adsorbed on {1 0 0} facets, it hinders Zn^{2+} and 2-MiM to attach to the surface of the crystals, and thus lead to the smaller crystals. By controlling the reaction time and the concentration of reactants, 400 nm TRD ZIF-8 nanoparticles can be also obtained (Fig. 2(b and g), Fig. S1). The concentrations of Zn^{2+} and 2-MiM influence the crystal growth rate and the reaction time decides the shape of ZIF-8. Because of the insufficient growth time, the crystals cannot evolve into rhombic dodecahedral particles and show as truncated rhombic dodecahedron at last. All of these samples present the characteristic XRD diffraction peaks of ZIF-8 (Fig. 1d), which confirms the successful formation of ZIF-8. In a word, the shapes and sizes of ZIF-8 can be controlled by varying the reaction conditions, which is important to design high performance STF with tunable mechanical properties. Here, the SiO_2 nanoparticles which are mostly used for preparing traditional S-STF are also synthesized for comparing the ST behavior of Z-STF and S-STF. As illustrated in Figs. 2(c, f), and S1, the microstructure of SiO_2 nanoparticles are spherical and have a similar particle size (~450 nm) to TRD ZIF-8.

Here, all the above particles are used to prepare the STFs and their rheological properties are compared. Similar to 300 nm TCZ-STF, the ST behaviors of 240 nm TCZ-STF and 400 nm TRDZ-STF become more intense when the volume fraction of the dispersing phase increases (Fig. 2(g and h)). The shear thickening properties of TCZ-STF are also regulated by the size of ZIF-8. Fig. 2i shows

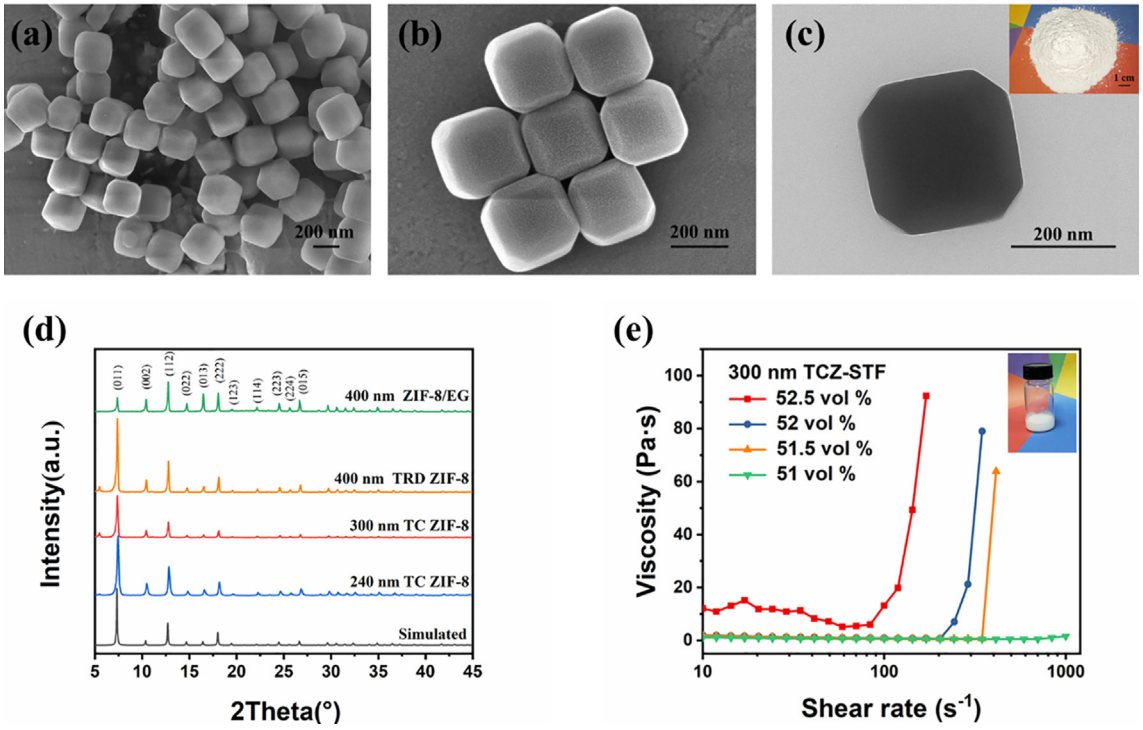

Fig. 1. SEM images (a), (b) and TEM image (c) of 300 nm TC ZIF-8. Inset: photograph of the 300 nm TC ZIF-8. XRD of ZIF-8 and ZIF-8/EG (d). The curve of viscosity versus shear rate for 300 nm TCZ-STF (e). Inset: photograph of 300 nm TCZ-STF.

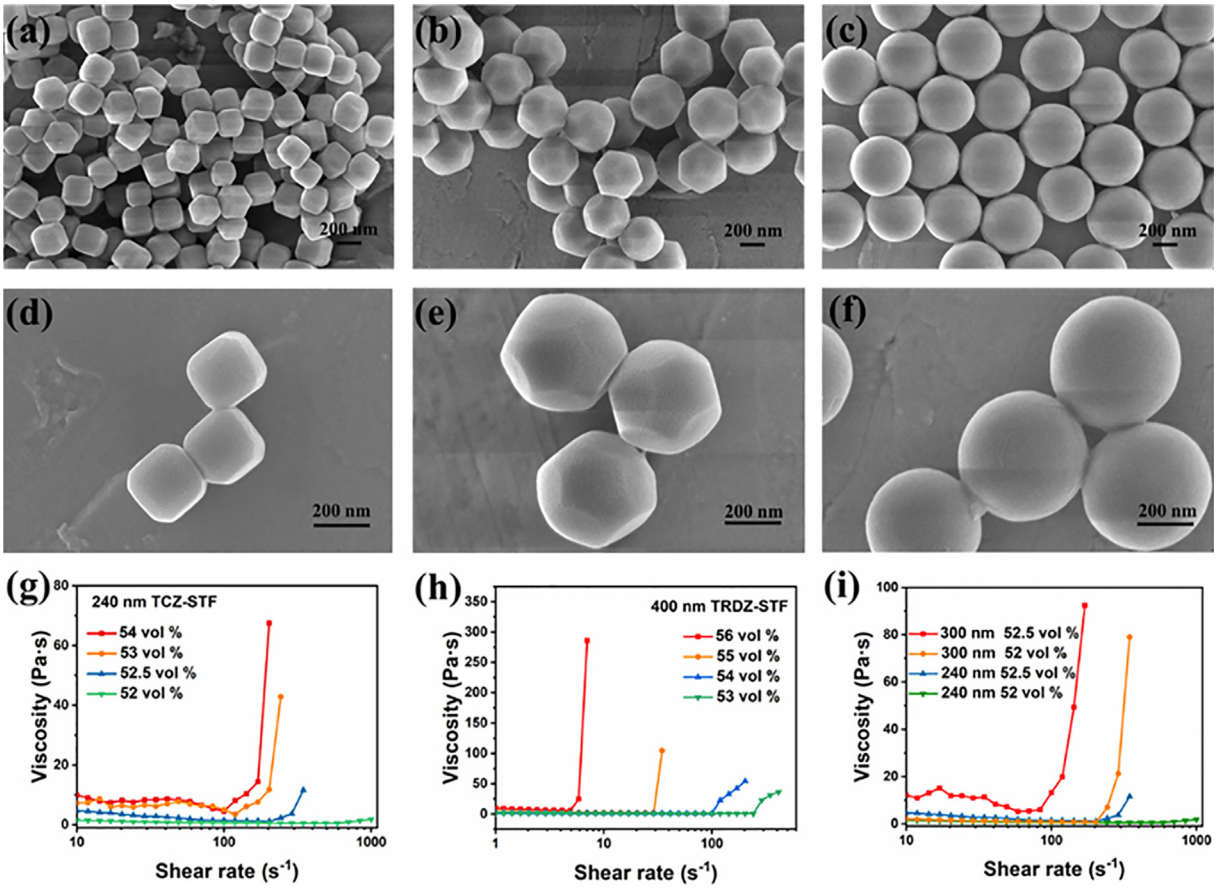

Fig. 2. SEM images of 240 nm TC ZIF-8 (a), (d); 400 nm TRD ZIF-8 (b), (e); 450 nm SiO_2 (c), (f). The curve of viscosity versus shear rate for 240 nm TCZ-STF (g), 400 nm TRDZ-STF (h) with different volume fractions. The curve of viscosity versus shear rate for TCZ-STF with different diameters at the same volume fraction (i).

the initial viscosity and the maximum viscosities improve with the increase of particle size, and the critical shear rate reduces with increasing of the particles' diameters. In summary, ST is more likely to occur at larger particle sizes and higher volume fractions, which agrees well with the previous research results [2,13,14].

The rheological properties of TRDZ-STF and S-STF, in which the dispersing phases have similar shape and diameter, are also compared (Fig. 3). Clearly, TRDZ-STF has lower critical shear rates and higher maximum viscosities versus S-STF at the same volume fractions. There are three possible reasons to illustrate this phenomenon. (1) In terms of microstructure, the TRD ZIF-8 is anisotropic compared with the SiO_2 sphere, which results in better ST

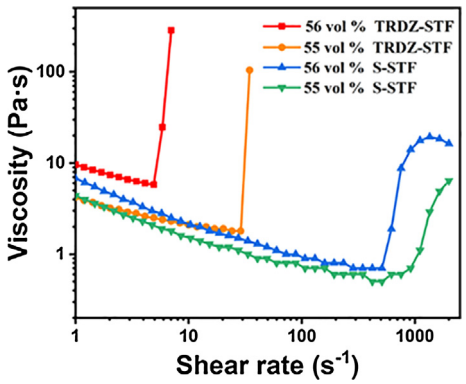

Fig. 3. The curve of viscosity versus shear rate for TRDZ-STF and S-STF, whereas ZIF-8 and SiO_2 have similar shape and size.

behavior [15]. Before the shear-thickening state, there are shear thinning regimes at both TRDZ-STF and S-STF. However, shear thinning behavior is weaker in TRDZ-STF. It is speculated that the weaker shear thinning behavior originates from the poorer relative sliding of anisotropic TRD ZIF-8 particles. (2) As a porous material, ZIF-8′s surface is rougher than SiO_2, which will induce larger friction when the particles contact under shearing and thus enhance the ST behavior. (3) Because of the adsorption properties of ZIF-8, EG can enter into the micropores of ZIF-8 and interact with ZIF-8 nanoparticles (Fig. 8a,b). This phenomenon increases the volume fraction of the dispersing phases and enhances the hydrodynamic forces between the ZIF-8 particles.

In this work, the presence of EG inside the micropores can be verified by various measurements. Firstly, as shown in XRD patterns (Fig. 1d), the characteristic peaks of ZIF-8/EG are same to pure ZIF-8, indicating that the crystal structure of ZIF-8 remains intact after mixing with EG and subsequent drying. It can also be observed that the relative intensities of the peaks changed. Especially, the intensity of the (0 1 1) and (0 1 3) changed dramatically. These changes demonstrate that the electron density within ZIF-8 may alter on account of EG incorporation [41,42]. However, it should be pointed out that partial decomposition of the sample would result in the change of XRD peak intensities as well. To investigate whether the framework was partial decomposed, the ZIF-8/EG was washed three times with ethanol and characterized SEM. The SEM images (Fig. S2) shows that the obtained ZIF-8 almost remain the shape and size of the pristine ZIF-8, which confirms the stability of the particles is very high. Thus, in combination with the results of XRD and SEM, the crystal structure of

ZIF-8 is remained intact during the Z-STF preparation and subsequent drying.

Fig. 4 shows the N_2 adsorption and desorption isotherms of the ZIF-8 and ZIF-8/EG. Both activated pristine ZIF-8 and ZIF-8/EG show type-I isotherms, indicating their microporous natures. The BET surface area of ZIF-8 is measured, it was 1426 $m^2 g^{-1}$ while the ZIF-8/EG decreases to 537 $m^2 g^{-1}$. This phenomenon results from the incorporation of EG. In addition, the pore volume decreases from 0.6379 $cm^3 g^{-1}$ to 0.1969 $cm^3 g^{-1}$ correspondingly. These reductions in the BET surface areas and the pore volumes must be derived from the EG incorporation. Therefore, the BET analysis confirms that the EG molecules can be incorporated into the ZIF-8 to give more hydrophilic surface.

The surface element compositions of pristine ZIF-8 and ZIF-8/EG are analyzed by XPS (Fig. 5). The atomic percentages of C, N, Zn, and O are summarized in the inset table. Both ZIF-8 and ZIF-8/EG clearly exhibit strong C1s, N1s, and Zn2p peaks. For pristine ZIF-8, there is a weak O1s peak in the spectrum, which may be resulted from the residual ethanol on the surface of the ZIF-8. For ZIF-8/EG, the intensity of the O1s peaks is obviously enhanced, and the atomic percentage of O in ZIF-8 and ZIF-8/EG are 4.3% and 8.95%, respectively. However, the atomic percentages of C, N, and Zn just show a slight decrease in ZIF-8/EG (Inset table). Thus, the EG is proven to be incorporated into ZIF-8 instead of wrapping the ZIF-8, to form a core–shell structure.

To further illustrate the incorporation of EG in ZIF-8′s micropores, thermogravimetric analysis (TGA) and FT-IR are analyzed. TGA (Fig. 6(a and c)) shows that the weight loss in ZIF-8/EG is larger than in ZIF-8 when they were heated under the same conditions. This phenomenon results from the decomposition of EG that incorporated in ZIF-8 micropores. The onset decomposition temperature (T_{onset}) is related to the decomposition mechanism. For pure EG, it begins to decompose at 40.5 °C, and they are decomposed completely when the temperature reaches to 169 °C. For pristine ZIF-8, the T_{onset} is around 459 °C and the total weight loss is about 71 wt% at the end of heating. As a comparison, the residual mass of ZIF-8/EG under the same heating conditions is about 64 wt % of the initial mass. The decomposition of ZIF-8/EG can be divided into three stages. The first stage starts at 40 °C and it is consistent with the T_{onset} of pure EG, the weight loss at this stage attributes to the decomposition of EG whose interaction with ZIF-8 is negligible. It is speculated that the EG molecules are located near the surface of the framework and the amount of this type of EG is small with only 4 wt% weight loss from TGA measurements. The second stage can be mainly ascribed to the decomposition of EG which has strong interaction with ZIF-8. There is a 20 wt% weight loss at this stage, which means that a large amount of EG is absorbed into the micropores of ZIF-8. The last stage occurs at 590 °C, which is dramatically higher than the onset decomposition temperatures of pure EG and pristine ZIF-8. It is supposed that the higher T_{onset} of ZIF-8/EG originates from the changed decomposition mechanism. This phenomenon indicates that EG can diffuse into the micropores of ZIF-8 and it interacts directly with ZIF-8. Owing to the interactions between ZIF-8 and EG, the ZIF-8/EG exhibits different thermal stability with its individual components. Such an increase of T_{onset} was also observed in the ZIF-8/ionic liquid system [30]. According to the TGA measurements, it should be pointed out that the BET surface area and pore volume of ZIF-8/EG (Fig. 4) are lower than the measured values, for the sample is activated at 100 °C for 5 h under vacuum before being tested, which must lead to partial escape of EG from the framework.

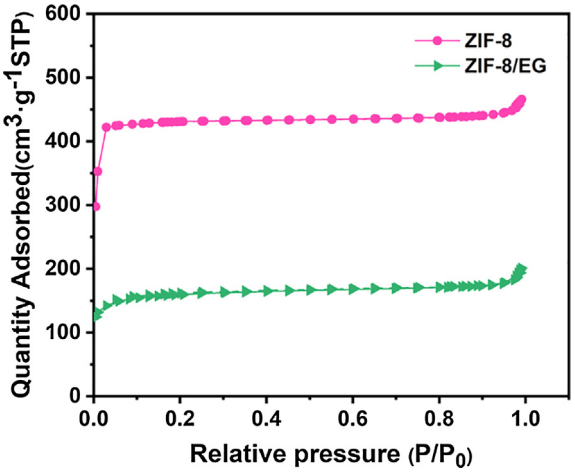

Fig. 4. N_2 adsorption-desorption isotherms of ZIF-8/EG and ZIF-8.

The interactions between ZIF-8 and EG can be manifested by changes in the FT-IR spectroscopy band positions. Here, the two different frequency regions, 4000–1800 (Fig. 6b) cm^{-1} and 1600–400 cm^{-1} (Fig. 6d) of the pure EG, ZIF-8, and ZIF-8/EG are compared. It is apparent that there are some blue and red shifts in the FT-IR spectra of EG's characteristic peaks in ZIF-8/EG. These shifts demonstrate that the EG interacts directly with ZIF-8. The characteristic peaks of pure EG and ZIF-8 are given in Tables 1 and S1. Bands of the EG at 2946, 2881, and 882 cm^{-1} show red shifts (by 17, 5, and 1 cm^{-1}, respectively), which can be ascribed to the limited vibration of EG molecules by the cages of ZIF-8. Other bands of EG exhibit blue shifts in ZIF-8/EG, to be specific, peaks located at 3384, 1086, 1042, and 523 cm^{-1} shift by 7, 2, 4, and 6 cm^{-1}, respectively, to the high wavenumber. According to Table 1, all of the X-O (X = C, H) stretching vibrations show blue shifts, it may be originating from the hydrogen bonds between EG and ZIF-8, O atom can draw electrons from ZIF-8 to enhance the X-O bonds. The existence of hydrogen bonds was also demonstrated by TGA measurements (Fig. 6(a and c)). Due to the association effect of the hydrogen bonds, the T_{onset} of EG (at the second stage) and ZIF-8 shifted to higher temperatures than their pure components. The assignment of partial peaks of ZIF-8 was also analyzed. The shifts in the characteristic bands of ZIF-8 in ZIF-8/EG can be observed as well (illustrated in Table S1). It indicates that EG is incorporated into the micropores of ZIF-8 and has interactions with ZIF-8. These interactions can be also evidenced by the changing intensities of the XRD peaks of ZIF-8/EG (Fig. 1d).

Here, the absorbed amount of EG in ZIF-8/EG was estimated to be 10.3 wt% for TRD ZIF-8 by TGA results (details of the calculation can be founded in Supporting Information). In other words, the 53 vol% and 55 vol% TRDZ-STF are equivalent to 56 vol%, 58 vol% S-STF respectively. As shown in Fig. 7a, TRDZ-STF still exhibits better ST effect than S-STF when the changes of volume fraction that originate from the incorporation EG into TRD ZIF-8 is excluded. This ST effect increasing phenomenon can be explained by the polyhedron morphology and rough surface of TRD ZIF-8. The polyhedron morphology leads to the poorer relative sliding of anisotropic TRD ZIF-8 particles than SiO_2 particles. The rough surface enhances the friction between the particles. Thus, TRDZ-STF exhibits weaker shear thinning behaviors, lower critical shear rates, and higher maximum viscosities. In addition, it is interesting to note that the initial viscosities of TRDZ-STF are significantly lower than that of S-STF, which may be responded to the stronger interaction between ZIF-8 with EG. The adsorption capacities of 300 nm and 240 nm TC ZIF-8 are estimated to be 13.1 wt% and 13.3 wt%, respectively, by the method of soaking-drying-weighing (details in Supporting Information). The adsorption capacity of 300 nm and 240 nm TC ZIF-8 is similar, thus the corresponding ST performance is mainly controlled by particle size. However, due to the smaller particle size (or larger specific surface area), the adsorption capacity of TC ZIF-8 is higher than TRD ZIF-8.

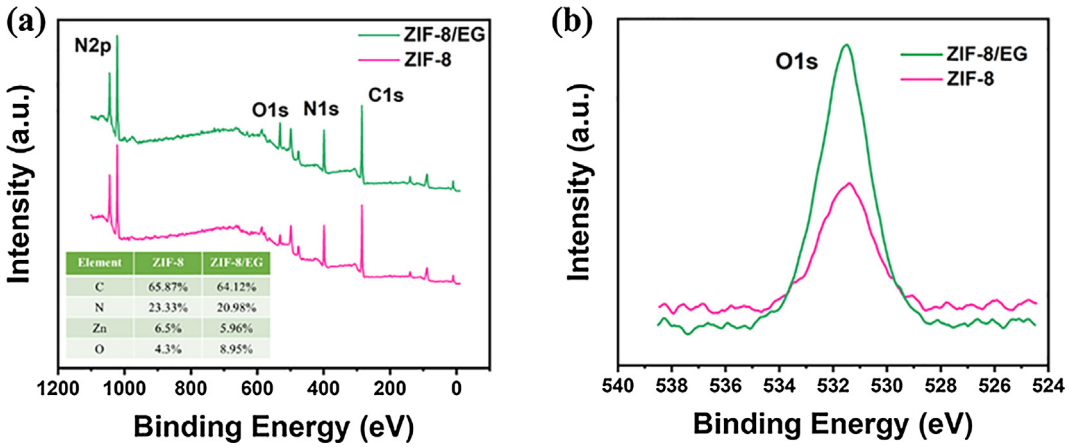

Fig. 5. Broad-range XPS spectra of ZIF-8 and ZIF-8/EG (a). Inset table: atomic percentages of C, N, Zn, O of ZIF-8 and ZIF-8/EG according to XPS measurements. The high resolution spectra for oxygen of ZIF-8 and ZIF-8/EG (b).

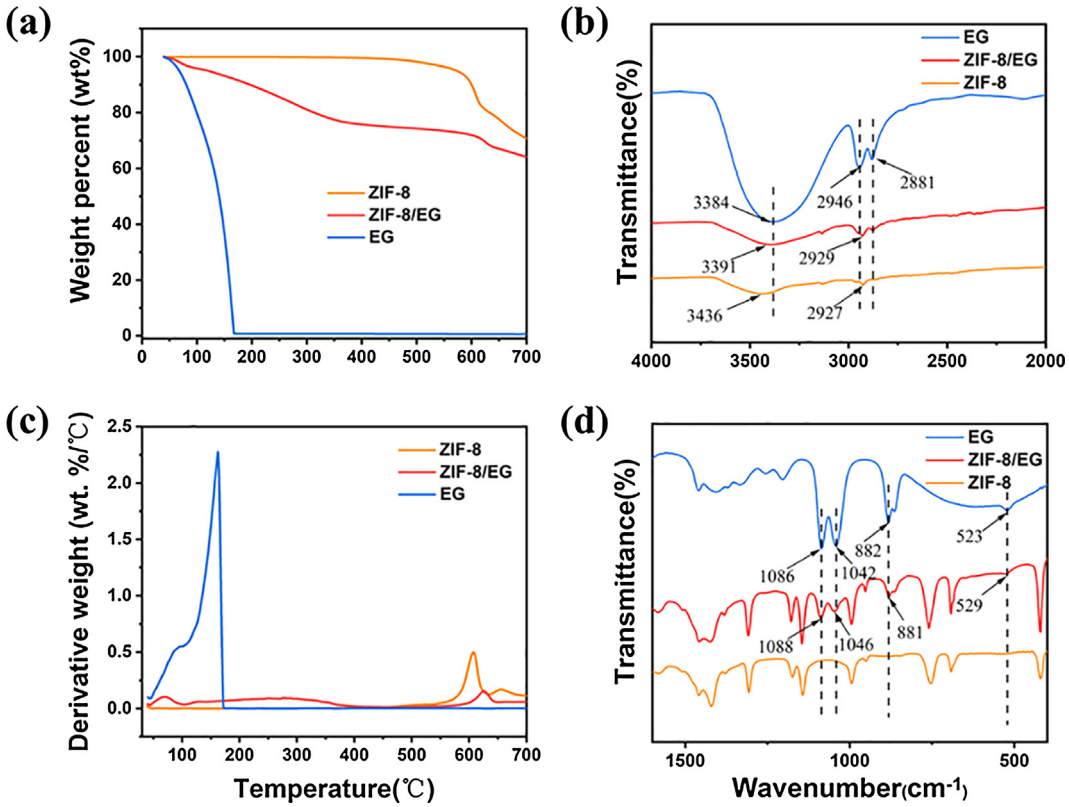

Fig. 6. TGA results of EG, ZIF-8, and ZIF-8/EG: change of weight percent (a) and derivative weight percent (c) with increasing temperature; FT-IR spectra of EG, ZIF-8, and ZIF-8/EG between 4000 and 1800 cm^{-1} (b) and 1600–400 cm^{-1} (d).

Table 1
Shifts in corresponding IR peaks of EG and ZIF-8/EG.

Assignment	EG (cm^{-1})	ZIF-8/EG (cm^{-1})
Stretching of O—H bonds	3384	3391
Antisymmetric stretching of C—H bonds	2946	2929
Symmetrical stretching of C—H bonds	2880	2876
Stretching of C—O bonds	1086	1088
Stretching of C—O bonds	1042	1047
In-plane bending of C—H bonds	882	881

The ST behaviors of TRDZ-STF and 300 nm TCZ-STF are also compared at the same net volume fraction (Fig. 7b). Although the TCZ-STF has a smaller particle size, it has higher initial viscosities and shows superior ST properties than TRDZ-STF. This phenomenon can be attributed to the different microstructure of the dispersing phases. The higher initial viscosities result from the poorer relative sliding of truncated cubic particles than truncated rhombic dodecahedron. According to the contact rheology model, the formation of friction contact networks was the main reason for the emergence of DST in STF [22–26]. As illustrated in Fig. 8c, truncated cubic particles and spherical particles have different contact modes during the shear thickening process (TRD ZIF-8 is simplified to a sphere). In the TCZ-STF, the interaction between particles is mainly depended on face-to-face contact, and it would restrict the particles' rotating and sliding. In the TRDZ-STF, the interaction between particles mainly carried out by point-to-

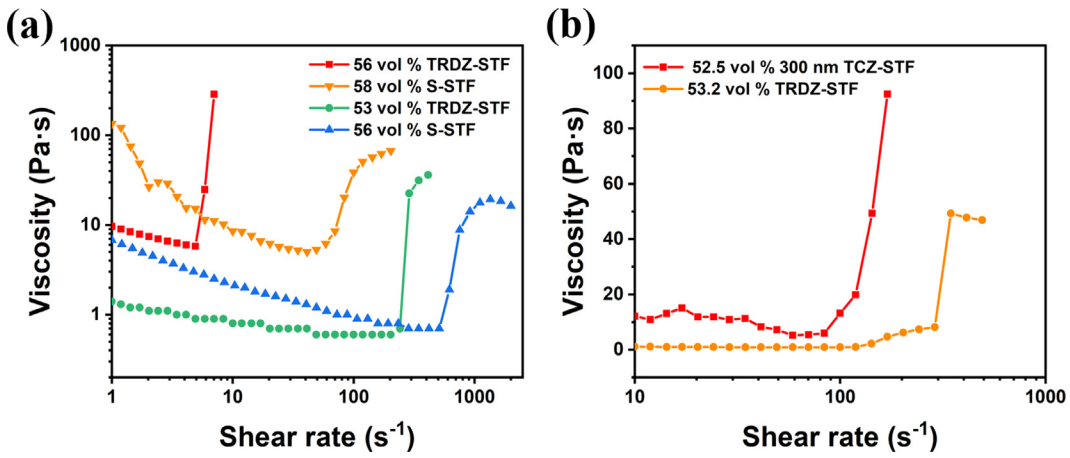

Fig. 7. The curve of viscosity versus shear rate for TRDZ-STF and S-STF at the same net volume fraction (a). The curve of viscosity versus shear rate for TRDZ-STF and 300 nm TCZ-STF at the same net volume fraction (b).

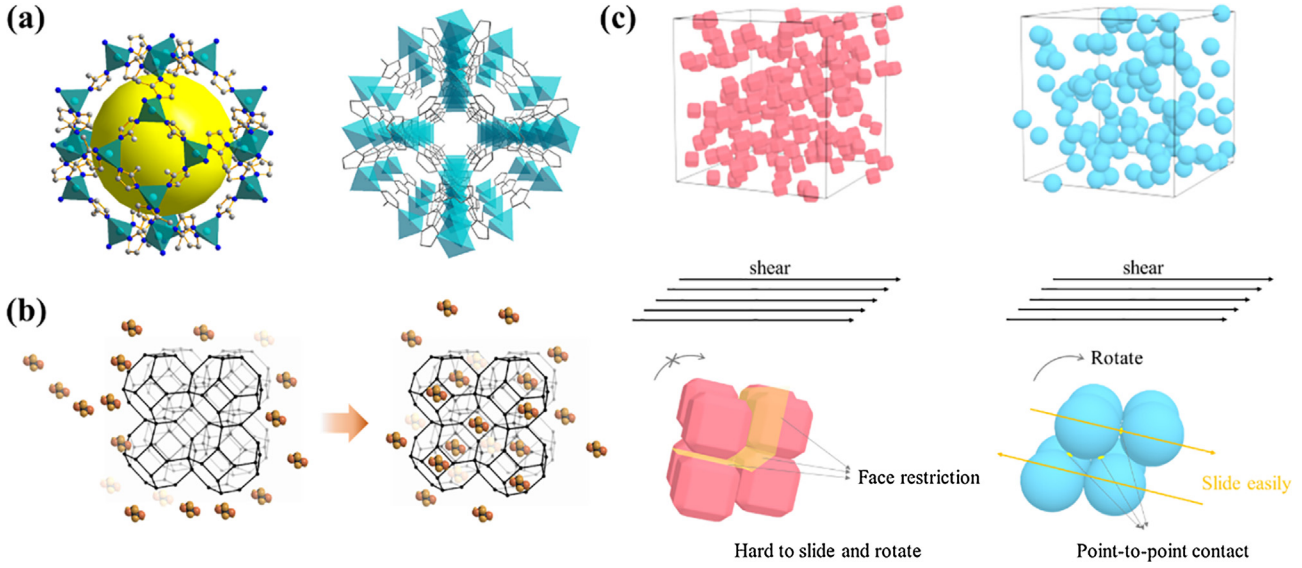

Fig. 8. Crystal structure of ZIF-8 (a). (yellow sphere on behalf of the cavity of ZIF-8). (Zinc, carbon, and nitrogen atoms are shown in light blue, gray, and dark blue, respectively.) (Hydrogen atoms are omitted for clarity). Representation of the incorporation of the EG into the micropores of ZIF-8 (b). The illustrations of interaction between nanoparticles in the STF (c). (For interpretation of the references to colour in this figure legend, the reader is referred to the web version of this article.)

point contact. As a result, the relative sliding of particles in the TCZ-STF system is more difficult, and the friction contact is easier to occur, thus the critical shear rates are lower.

As the shear rate increases, the friction gradually plays a dominant role in the system, forming a frictional contact network, and package structures evolved from the aggregations. At this stage, the frictional contact network formed by truncated cubic nanoparticles has a stronger structure, for the relative sliding of truncated cubic particles is poorer than sphere particles. In addition, the solvent molecules are restricted within the package structures, leading to the dramatical increase of the effective volume fraction of the dispersing phase. The frictional contact network and the solvent molecules restricted within the package structures lead the flowing to be more difficultly and increase the shear stress. In other words, the viscosity of the system rises tempestuously.

4. Conclusions

In this work, ZIF-8 nanoparticles with different sizes and shapes were synthesized and dispersed into the EG for the preparation of high performance STFs. The characteristics of ZIF-8 particles can be controlled by varying the reaction conditions. The ZIF-8′s structure dependent ST behaviors of Z-STF were systematically investigated and the enhancing mechanism was discussed. Firstly, the TRDZ-STF exhibits better ST properties than S-STF, for EG can enter into the micropores of ZIF-8 and show high interactions with ZIF-8, which increases the volume fraction of the dispersing phases and enhances the hydrodynamic forces between the ZIF-8. Then, the ST behaviors of TCZ-STF and TRDZ-STF were compared at the same net volume fraction. The poor relative sliding of truncated cubic particles would lead to two results: (1) the formation of frictional contact network in TCZ-STF is easier than in TRDZ-STF, thus the critical shear rates are lower in TCZ-STF; (2) the formed frictional contact network is more robust in TCZ-STF, which means the TCZ-STF shows higher maximum viscosities. As a result, TCZ-STF shows superior ST properties than TRDZ-STF. This work provides a new ZIF-8 based STF system which supplies a good understanding of the relationship between ST behavior and particles' structure. In addition, it is expected that the introduction of ZIF-8 into STF will broaden the application range of STF.

Acknowledgements

Financial supports from the National Natural Science Foundation of China (Grant No. 11772320, 11802303, 11822209), the Strategic Priority Research Program of the Chinese Academy of Sciences (Grant No. XDB22040502), and China Postdoctoral Science Foundation (2019T120544) are gratefully acknowledged. This study was also supported by the Collaborative Innovation Center of Suzhou Nano Science and Technology.

Appendix A. Supplementary material

Supplementary data to this article can be found online at https://doi.org/10.1016/j.apt.2019.10.001.

References

[1] C. Hu, J. Liu, Y. Wu, K.R. West, O.A. Scherman, Cucurbit [8] uril-regulated colloidal dispersions exhibiting photocontrolled rheological behavior, Small 14 (2018) 1703352.
[2] M. Liu, W. Jian, S. Wang, S. Xuan, L. Bai, M. Sang, X. Gong, Shear thickening fluid with tunable structural colors, Smart. Mater. Struct. 27 (2018), 095012.
[3] M. Hasanzadeh, V. Mottaghitalab, M. Rezaei, Rheological and viscoelastic behavior of concentrated colloidal suspensions of silica nanoparticles: A response surface methodology approach, Adv. Powder Technol. 26 (2015) 1570–1577.
[4] A.F. Ávila, A.M. de Oliveira, S.G. Leão, M.G. Martins, Aramid fabric/nano-size dual phase shear thickening fluid composites response to ballistic impact, Compos. Part. A Appl. Sci. Manuf. 112 (2018) 468–474.
[5] K. Liu, C.-F. Cheng, L. Zhou, F. Zou, W. Liang, M. Wang, Y. Zhu, A shear thickening fluid based impact resistant electrolyte for safe Li-ion batteries, J. Power Sources 423 (2019) 297–304.
[6] S. Gürgen, A. Sert, Polishing operation of a steel bar in a shear thickening fluid medium, Compos. Part B Eng. 175 (2019), 107127.
[7] S. Arora, A. Majumdar, B.S. Butola, Structure induced effectiveness of shear thickening fluid for modulating impact resistance of UHMWPE fabrics, Compos. Struct. 210 (2019) 41–48.
[8] S. Gürgen, M.C. Kuşhan, W. Li, Shear thickening fluids in protective applications: A review, Prog. Polym. Sci. 75 (2017) 48–72.
[9] C.D. Cwalina, C.M. McCutcheon, R.D. Dombrowski, N.J. Wagner, Engineering enhanced cut and puncture resistance into the thermal micrometeoroid garment (TMG) using shear thickening fluid (STF) – Armor™ absorber layers, Compos. Sci. Technol. 131 (2016) 61–66.
[10] S. Gürgen, M.C. Kuşhan, The stab resistance of fabrics impregnated with shear thickening fluids including various particle size of additives, Compos. Part. A-Appl. S. 94 (2017) 50–60.
[11] R. Sharma, S.K. Verma, I. Biswas, D. Bhattacharjee, P. Kamal, Effect of thermal surface activation of silica nanoparticles on the rheological behavior of shear thickening fluid, Mater. Res. Express 6 (2019), 065710.
[12] Z. Tan, H. Ma, H. Zhou, X. Han, C. Cho, The influence of graphene on the dynamic mechanical behaviour of shear thickening fluids, Adv. Powder Technol. 30 (2019) 2416–2421.
[13] B.J. Maranzano, N.J. Wagner, The effects of particle size on reversible shear thickening of concentrated colloidal dispersions, J. Chem. Phys. 114 (2001) 10514–10527.
[14] M. Yu, X. Qiao, X. Dong, K. Sun, Shear thickening effect of the suspensions of silica nanoparticles in PEG with different particle size, concentration, and shear, Colloid Polym. Sci. 296 (2018) 1119–1126.
[15] R.G. Egres, N.J. Wagner, The rheology and microstructure of acicular precipitated calcium carbonate colloidal suspensions through the shear thickening transition, J. Rheol. 49 (2005) 719–746.
[16] R. Seto, R. Mari, J.F. Morris, M.M. Denn, Discontinuous shear thickening of frictional hard-sphere suspensions, Phys. Rev. Lett. 111 (2013), 218301.
[17] R. Mari, R. Seto, J.F. Morris, M.M. Denn, Shear thickening, frictionless and frictional rheologies in non-Brownian suspensions, J. Rheol. 58 (2014) 1693–1724.
[18] Q. He, X. Gong, S. Xuan, W. Jiang, Q. Chen, Shear thickening of suspensions of porous silica nanoparticles, J. Mater. Sci. 50 (2015) 6041–6049.
[19] J.R. Melrose, R.C. Ball, Continuous shear thickening transitions in model concentrated colloids-The role of interparticle forces, J. Rheol. 2004 (48) (2004) 937–960.
[20] J.R. Melrose, R.C. Ball, "Contact networks" in continuously shear thickening colloids, J. Rheol. 48 (2004) 961–978.
[21] A.A. Catherall, J.R. Melrose, R.C. Ball, Shear thickening and order-disorder effects in concentrated colloids at high shear rates, J. Rheol. 44 (2000) 1–25.
[22] K. Chen, Y. Wang, S. Xuan, S. Cao, X. Gong, Contribution of frictional contact during steady and oscillatory shear in the discontinuous shear thickening fluid, Smart Mater. Struct. 28 (2019), 045009.
[23] L.E. Edens, S. Pednekar, J.F. Morris, G.K. Schenter, A.E. Clark, J. Chun, Global topology of contact force networks: Insight into shear thickening suspensions, Phys. Rev. E 99 (2019), 012607.
[24] S. Pednekar, J. Chun, J.F. Morris, Simulation of shear thickening in attractive colloidal suspensions, Soft Matter 13 (2017) 1773–1779.
[25] L.C. Hsiao, S. Jamali, E. Glynos, P.F. Green, R.G. Larson, M.J. Solomon, Rheological state diagrams for rough colloids in shear flow, Phys. Rev. Lett. 119 (2017), 158001.
[26] C.P. Hsu, S.N. Ramakrishna, M. Zanini, N.D. Spencer, L. Isa, Roughness-dependent tribology effects on discontinuous shear thickening, Proc. Natl. Acad. Sci. U. S. A. 115 (2018) 5117–5122.
[27] J. Cousin Saint Remi, T. Rémy, V. Van Hunskerken, S. van de Perre, T. Duerinck, M. Maes, D. De Vos, E. Gobechiya, C.E.A. Kirschhock, G.V. Baron, J.F.M. Denayer, Biobutanol separation with the metal–organic framework ZIF-8, ChemSusChem 4 (2011) 1074–1077.
[28] J. Pérez-Pellitero, H. Amrouche, F.R. Siperstein, G. Pirngruber, C. Nieto-Draghi, G. Chaplais, A. Simon-Masseron, D. Bazer-Bachi, D. Peralta, N. Bats, Adsorption of CO_2, CH_4, and N_2 on zeolitic imidazolate frameworks: experiments and simulations, Chem. Eur. J. 16 (2010) 1560–1571.
[29] J.C. Tan, T.D. Bennett, A.K. Cheetham, Chemical structure, network topology, and porosity effects on the mechanical properties of zeolitic imidazolate frameworks, Proc. Natl. Acad. Sci. U. S. A. 107 (2010) 9938–9943.
[30] M. Zeeshan, V. Nozari, M.B. Yagci, T. Isık, U. Unal, V. Ortalan, S. Keskin, A. Uzun, Core–shell type ionic liquid/metal organic framework composite: an Exceptionally high CO_2/CH_4 selectivity, J. Am. Chem. Soc. 140 (2018) 10113–10116.
[31] T. Wu, J. Lucero, M.A. Sinnwell, P.K. Thallapally, M.A. Carreon, Recovery of xenon from air over ZIF-8 membranes, Chem. Commun. 54 (2018) 8976–8979.
[32] X. Ma, R.J. Swaidan, Y. Wang, C.E. Hsiung, Y. Han, I. Pinnau, Highly compatible hydroxyl-functionalized microporous polyimide-ZIF-8 mixed matrix membranes for energy efficient propylene/propane separation, ACS Appl. Nano Mater. 1 (2018) 3541–3547.
[33] K.S. Park, Z. Ni, A.P. Côté, J.Y. Choi, R. Huang, F.J. Uribe-Romo, H.K. Chae, M. O'Keeffe, O.M. Yaghi, Exceptional chemical and thermal stability of zeolitic imidazolate frameworks, P. Natl. Acad. Sci. U. S. A. 103 (2006) 10186–10191.
[34] C. Avci, I. Imaz, A. Carné-Sánchez, J.A. Pariente, N. Tasios, J. Pérez-Carvajal, M.I. Alonso, A. Blanco, M. Dijkstra, C. López, Self-assembly of polyhedral metal–organic framework particles into three-dimensional ordered superstructures, Nat. Chem. 10 (2018) 78–84.
[35] S. Watanabe, S. Ohsaki, A. Fukuta, T. Hanafusa, K. Takada, H. Tanaka, T. Maki, K. Mae, M.T. Miyahara, Characterization of mixing performance in a microreactor and its application to the synthesis of porous coordination polymer particles, Adv. Powder Technol. 28 (2017) 3104–3110.
[36] Y. Pan, D. Heryadi, F. Zhou, L. Zhao, G. Lestari, H. Su, Z. Lai, Tuning the crystal morphology and size of zeolitic imidazolate framework-8 in aqueous solution by surfactants, CrystEngComm 13 (2011) 6937–6940.
[37] Y. Jiang, H. Liu, X. Tan, L. Guo, J. Zhang, S. Liu, Y. Guo, J. Zhang, H. Wang, W. Chu, Monoclinic ZIF-8 nanosheet-derived 2D carbon nanosheets as sulfur immobilizer for high-performance lithium sulfur batteries, ACS Appl. Mater. Inter. 9 (2017) 25239–25249.
[38] G. Ortiz, H. Nouali, C. Marichal, G. Chaplais, J. Patarin, Versatile energetic behavior of ZIF-8 upon high pressure intrusion–extrusion of aqueous electrolyte solutions, J. Phys. Chem. C 118 (2014) 7321–7328.
[39] J. Cravillon, R. Nayuk, S. Springer, A. Feldhoff, K. Huber, M. Wiebcke, Controlling zeolitic imidazolate framework nano-and microcrystal formation: insight into crystal growth by time-resolved in situ static light scattering, Chem. Mater. 23 (2011) 2130–2141.
[40] J. Cravillon, C.A. Schröder, H. Bux, A. Rothkirch, J. Caro, M. Wiebcke, Formate modulated solvothermal synthesis of ZIF-8 investigated using time-resolved in situ X-ray diffraction and scanning electron microscopy, CrystEngComm 14 (2012) 492–498.
[41] K. Fujie, T. Yamada, R. Ikeda, H. Kitagawa, Introduction of an ionic liquid into the micropores of a metal-organic framework and its anomalous phase behavior, Angew. Chem. Int. Ed. 53 (2014) 11302–11305.
[42] F.P. Kinik, C. Altintas, V. Balci, B. Koyuturk, A. Uzun, S. Keskin, [BMIM][PF_6] incorporation doubles CO_2 selectivity of ZIF-8: elucidation of interactions and their consequences on performance, ACS Appl. Mater. Inter. 8 (2016) 30992–31005.